

# Large-scale CO ( $J=4-3$ ) mapping toward the Orion-A giant molecular cloud

Shun ISHII,<sup>1,\*</sup> Masumichi SETA,<sup>1,†</sup> Makoto NAGAI,<sup>1,2</sup> Yusuke MIYAMOTO,<sup>1,3</sup>  
Naomasa NAKAI,<sup>1,2</sup> Taketo NAGASAKI,<sup>1,4</sup> Hitoshi ARAI,<sup>1,3</sup> Hiroaki IMADA,<sup>1</sup>  
Naoki MIYAGAWA,<sup>1</sup> Hiroyuki MAEZAWA,<sup>5</sup> Hideki MAHASHI,<sup>1</sup>  
Leonardo BRONFMAN,<sup>6</sup> and Ricardo FINGER<sup>6</sup>

<sup>1</sup>Division of Physics, Faculty of Pure and Applied Sciences, University of Tsukuba, 1-1-1 Tennodai, Tsukuba, Ibaraki 305-8571, Japan

<sup>2</sup>Center for Integrated Research in Fundamental Science and Technology (CiRfSE), University of Tsukuba, 1-1-1 Tennodai, Tsukuba, Ibaraki 305-8571, Japan

<sup>3</sup>Nobeyama Radio Observatory, NAOJ, 462-2 Nobeyama, Minamimaki, Nagano 384-1305, Japan

<sup>4</sup>High Energy Accelerator Research Organization (KEK), 1-1 Oho, Tsukuba, Ibaraki 305-0801, Japan

<sup>5</sup>The School of Science, Osaka Prefecture University, 1-1 Gakuen-cho, Naka-ku, Sakai, Osaka 599-8531, Japan

<sup>6</sup>Departamento de Astronomía, Universidad de Chile, Casilla 36-D, Santiago, Chile

\*E-mail: [sishi@ioa.s.u-tokyo.ac.jp](mailto:sishi@ioa.s.u-tokyo.ac.jp)

†Present address: Institute of Astronomy, The University of Tokyo, 2-21-1 Osawa, Mitaka, Tokyo 181-0015, Japan

‡School of Science and Technology, Kwansei Gakuin University, 2-1 Gakuen, Sanda, Hyogo 669-1337, Japan

Received 2015 March 3; Accepted 2015 October 31

## Abstract

We have mapped the Orion-A giant molecular cloud in the CO ( $J=4-3$ ) line with the Tsukuba 30 cm submillimeter telescope. The map covered a  $7.125\text{ deg}^2$  area with a  $9'$  resolution, including main components of the cloud such as the Orion Nebula, OMC-2/3, and L1641-N. The most intense emission was detected toward the Orion KL region. The integrated intensity ratio between CO ( $J=4-3$ ) and CO ( $J=1-0$ ) was derived using data from the Columbia–Universidad de Chile CO survey, which was carried out with a comparable angular resolution. The ratio was  $r_{4-3/1-0} \sim 0.2$  in the southern region of the cloud and 0.4–0.8 at star forming regions. We found a trend that the ratio shows higher values at the edges of the cloud. In particular, the ratio at the northeastern edge of the cloud at  $(l, b) \approx (208^\circ.375, -19^\circ.0)$  shows the highest value of 1.1. The physical condition of the molecular gas in the cloud was estimated by non-LTE calculation. The result indicates that the kinetic temperature has a gradient from north ( $T_{\text{kin}} = 80\text{ K}$ ) to south (20 K). The estimation shows that the gas associated with the edge of the cloud is warm ( $T_{\text{kin}} \sim 60\text{ K}$ ), dense ( $n_{\text{H}_2} \sim 10^4\text{ cm}^{-3}$ ), and optically thin, which may be explained by heating and sweeping of interstellar materials from OB clusters.

**Key words:** ISM: clouds — ISM: individual objects (Orion) — submillimeter: ISM

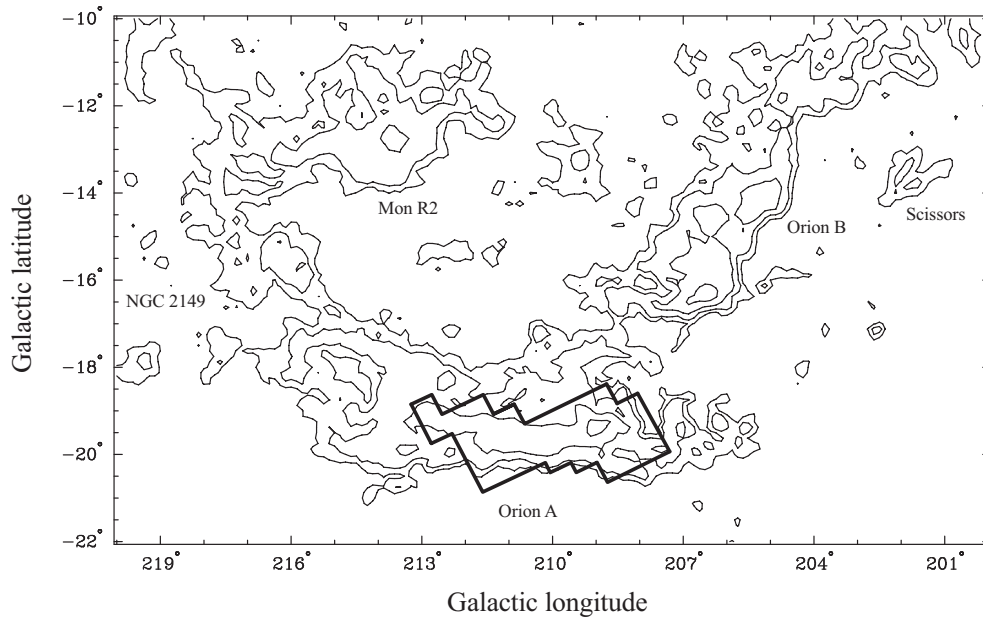


**Fig. 1.** The distribution of the Orion–Monoceros molecular complex traced by the integrated intensity of the  $^{12}\text{CO}$  ( $J=1-0$ ) emission (Wilson et al. 2005). The contour levels are 3, 9, 27, and  $81 \text{ K km s}^{-1}$ . The mapping region of the  $^{12}\text{CO}$  ( $J=4-3$ ) line is indicated with thick lines.

## 1 Introduction

Star-forming activity in galaxies is closely related to the distribution and physical conditions of giant molecular clouds (GMCs). The large-scale surveys, which are represented by the Columbia–Universidad de Chile CO surveys, have investigated the global distribution of GMCs, structures of molecular gas both in space and velocity, and the total amount of molecular gas in the Milky Way (Dame et al. 1987, 2001; Bronfman et al. 1988). In addition, the detailed structures, the size, and the mass of individual galactic regions and GMCs are also revealed by observations of  $^{12}\text{CO}$  ( $J=1-0$ ),  $^{12}\text{CO}$  ( $J=2-1$ ), and  $^{13}\text{CO}$  ( $J=1-0$ ) lines, mostly with small and middle-sized telescopes (e.g., Sakamoto et al. 1994; Dobashi et al. 1994; Mizuno et al. 1995; Oka et al. 1998). Nevertheless, the global distribution of physical conditions such as temperature, density, and column density over the GMCs is still unclear because such observations have been carried out only in lower transition lines of CO.

We made survey observations in the  $^{12}\text{CO}$  ( $J=4-3$ ) emission line toward the Orion-A GMC to derive the physical properties of molecular gas over the GMC, with the same angular resolution of  $9'$  as those of the previous  $^{12}\text{CO}$  ( $J=1-0$ ) and  $^{12}\text{CO}$  ( $J=2-1$ ) observations (Maddalena et al. 1986; Wilson et al. 2005; Sakamoto et al. 1994). This enables us to directly compare the intensities of the different CO transitions and thus to estimate the temperature and the column and volume densities of the gas. The Orion-A GMC is the most suitable site for studying massive star formation because of its close distance to the sun ( $\sim 420 \text{ pc}$ ; Hirota et al. 2007; Menten

et al. 2007; Kim et al. 2008). Star formation is ongoing in the integral-shaped filament with an extent of  $\sim 2^\circ$  ( $\sim 15 \text{ pc}$ ), along the north–south direction, which consists of several components such as OMC-1 to OMC-5 (Johnstone & Bally 1999, 2006). Maddalena et al. (1986) surveyed the Orion–Monoceros region in the  $^{12}\text{CO}$  ( $J=1-0$ ) line with the 1.2 m telescope [ $8.7'$  of half-power beam width (HPBW)] as a part of the Columbia–Universidad de Chile CO survey. They determined the spatial extent of three GMCs, Orion A, Orion B, and Mon R2 (figure 1), where the mass was evaluated to be  $1.0 \times 10^5$ ,  $0.8 \times 10^5$ , and  $0.9 \times 10^5 M_\odot$ , respectively, comparing with the virial mass, the local thermodynamic equilibrium (LTE) mass, and the CO mass. Wilson et al. (2005) re-observed the same region in the same line with uniform sampling. Sakamoto et al. (1994) mapped the Orion-A and -B GMCs in the  $^{12}\text{CO}$  ( $J=2-1$ ) line using the Tokyo–NRO 60 cm survey telescope.<sup>1</sup> The  $^{12}\text{CO}$  ( $J=2-1$ )/ $^{12}\text{CO}$  ( $J=1-0$ ) intensity ratio was almost unity on the main structure of the clouds, H II regions, reflection nebulae, and the western edge of the clouds. They estimated the gas density over the GMCs using the intensity ratio by the large velocity gradient method, and the densities of the main and peripheral regions were  $\sim 3 \times 10^3 \text{ cm}^{-3}$  and  $\sim 2 \times 10^2 \text{ cm}^{-3}$ , respectively. Bally et al. (1987) surveyed the Orion-A GMC in the  $^{13}\text{CO}$  ( $J=1-0$ ) line with the AT&T Bell Laboratories 7 m telescope ( $1.8'$  of angular resolution). The  $^{13}\text{CO}$  ( $J=1-0$ ) map revealed that the overall

<sup>1</sup> The telescope was renamed the AMANOGAWA telescope in 2010 after an upgrade to a new 2SB receiver in 2007 (Nakajima et al. 2007; Yoda et al. 2010).

structure of the cloud is filamentary. This morphology indicates that the northern part of Orion A is compressed and supports massive star formation. The southern part is, however, diffuse and exhibits chaotic spatial and velocity structure, supporting only intermediate- to low-mass star formation. The integral-shaped filament is about 0.5 pc wide, at least 13 pc long, and has a mass of  $5 \times 10^3 M_{\odot}$  estimated from the  $^{13}\text{CO}$  ( $J=1-0$ ) data. Bally et al. (1987) explained these properties as resulting from the compression of the interstellar medium by a superbubble driven by the Orion OB association. Nagahama et al. (1998) also mapped the Orion-A GMC in the  $^{13}\text{CO}$  ( $J=1-0$ ) line and found 39 filamentary structures. Nishimura et al. (2015) mapped the same cloud in  $^{12}\text{CO}$  ( $J=2-1$ ),  $^{13}\text{CO}$  ( $J=2-1$ ), and  $\text{C}^{18}\text{O}$  ( $J=2-1$ ) and derived temperature and density by comparing their data as well as  $^{12}\text{CO}$  ( $J=1-0$ ),  $^{13}\text{CO}$  ( $J=1-0$ ), and  $\text{C}^{18}\text{O}$  ( $J=1-0$ ) data. They found a temperature gradient along the cloud ridge. Mapping observations of  $^{12}\text{CO}$  ( $J=3-2$ ) and  $[\text{C I}](^3\text{P}_1-^3\text{P}_0)$  carried out by Ikeda et al. (1999) with the Mt. Fuji submillimeter-wave telescope found that the distribution of  $[\text{C I}](^3\text{P}_1-^3\text{P}_0)$  is quite similar to that of  $^{13}\text{CO}$  ( $J=1-0$ ).

The GMC accompanies the Orion OB1 association, which is known as a typical stellar cluster (Brown et al. 1994). The association consists of several subgroups named OB1a–d from the northwest of the GMC. The numbers of stars in subgroups a, b, c, and d are 53, 31, 34, and 3, respectively. The ages of the subgroups have been thought to be mostly older from the northwest. OB1a, the oldest subgroup is 11 Myr old. OB1b and Ob1c were formed 1–5 Myr ago in the close generation, while Brown, de Geus, and de Zeeuw (1994) determined that the OB1c subgroup is older than the OB1b subgroup. The OB1d subgroup, located nearest to the Orion-A GMC and known as the Orion Nebula and NGC 1976, was estimated as less than 1 Myr old. The differences in ages and evolutionary stages of the Orion-A OB1 subgroups and the GMC can be interpreted as the result of sequential star formation, as suggested by Elmegreen and Lada (1977). The global star formation history of the Orion OB1 association and the GMC is therefore crucial to understanding the formation of a stellar cluster and triggered star formation scenarios.

Several observations indicated that there are gradients in morphology, in velocity structure, and in intensity of emission lines over the Orion-A GMC. The temperature-weighted velocity maps of the  $^{12}\text{CO}$  lines traced the substantial velocity gradient from the north ( $V_{\text{LSR}} = 11 \text{ km s}^{-1}$ ) to the south ( $V_{\text{LSR}} = 3 \text{ km s}^{-1}$ ) over the GMC (Wilson et al. 2005; Shimajiri et al. 2011; Nishimura et al. 2015). The origin of the velocity gradient has been attributed to rotation of the GMC (Kutner et al. 1977;

Maddalena et al. 1986) or to large-scale expansion driven by the stellar winds of the Orion OB1 association (Bally et al. 1987). Wilson et al. (2005) also advocated the latter, because there was evidence of interaction between the Orion OB1 association and the Orion-A GMC. For example, there are sharp  $^{12}\text{CO}$  ( $J=1-0$ ) intensity drops and velocity shifts with respect to the main component of the cloud at the edge of the cloud, which are attributed to expanding shells driven by an H II region, the Orion Nebula, excited by young massive stars in OB1c. The integrated intensity ratio of  $[\text{C I}](^3\text{P}_1-^3\text{P}_0)/^{12}\text{CO}$  ( $J=3-2$ ) also shows a gradient from north ( $\sim 0.1$ ) to south ( $\sim 1.2$ ; Ikeda et al. 2002). The gradient of the  $[\text{C I}](^3\text{P}_1-^3\text{P}_0)/^{12}\text{CO}$  ( $J=3-2$ ) ratio was interpreted as a consequence of the temperature gradient. In addition, heating by the Orion OB1 association may be responsible for the global gradient. The diffuse interstellar material may have been swept up and accumulated by the OB1 association through the processes that made the temperature and intensity gradients in the Orion-A GMC. Some authors suggested that the triggered star formation is occurring through interaction between the Orion OB1 association and the Orion-A GMC (Wilson et al. 2005; Shimajiri et al. 2011).

In the next section, we describe the details of the observations. The results of the survey, the distribution and velocities over the GMC, are presented in section 3. In section 4, we analyze the physical properties of the molecular gas using the  $^{12}\text{CO}$  ( $J=4-3$ ) data with other archival data, and also discuss the triggered star formation in the GMC. In the last section, we summarize the results of this paper. Throughout this paper, we adopt 418 pc (Kim et al. 2008) as the distance of Orion KL, at which  $1'$  and  $1''$  correspond to 0.12 pc and  $2.0 \times 10^{-3}$  pc, respectively. The velocity used here is expressed with respect to the local standard of rest (LSR) in the radio definition.

## 2 Observations

The observations of  $^{12}\text{CO}$  ( $J=4-3$ ) were made with the Tsukuba 30 cm submillimeter telescope of the University of Tsukuba during 2011 September and October. The 30 cm telescope (figure 2) is a transportable submillimeter telescope developed for a Galactic plane survey in the CO ( $J=4-3$ ) line at 461.04077 GHz and  $[\text{C I}](^3\text{P}_1-^3\text{P}_0)$  line at 492.16065 GHz from the Dome Fuji station on the Antarctic plateau (Seta et al. 2012; Ishii et al. 2013). We operated the telescope at a site 4400 m above sea level at Parinacota in northern Chile for test observations and carried out the present survey of the Orion-A GMC. The site is located at  $18^{\circ}12' \text{ S}$ ,  $69^{\circ}16' \text{ W}$ . The telescope has a 30 cm-diameter main reflector and  $\text{HPBW} = 9.4 \pm 0.4$  at 461 GHz, which was measured by scanning the Sun

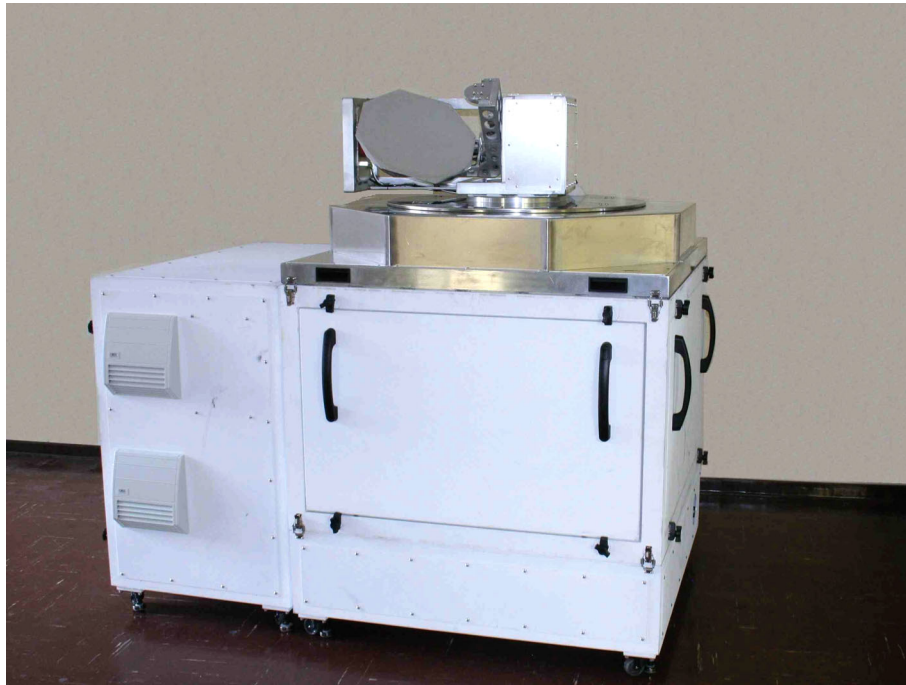


Fig. 2. Photograph of the Tsukuba 30 cm submillimeter telescope which is of the offset Cassegrain design. (Color online)

and corresponds to 1.1 pc at the distance of Orion KL, 418 pc. The beam size is almost equal to those of the Columbia-CfA and Universidad de Chile 1.2 m telescopes at the frequency of CO ( $J=1-0$ ) (Dame et al. 2001) and the AMANOGAWA telescope at the CO ( $J=2-1$ ) frequency (Yoda et al. 2010). The forward coupling efficiency was estimated by observing the new moon to be  $\eta_{\text{Moon}} = 87\% \pm 10\%$  by assuming the brightness temperature of the new moon to be 110 K at 461 GHz (Linsky 1973). The sidelobe level of the beam of the 30 cm telescope was less than  $-18$  dB relative to the peak of the main beam. In this condition we can regard the forward coupling efficiency as the main beam efficiency  $\eta_{\text{mb}}$  and the difference between  $\eta_{\text{Moon}}$  and  $\eta_{\text{mb}}$  is estimated to be  $\lesssim 1\%$  (Yoda et al. 2010). We adopt  $\eta_{\text{mb}} \approx \eta_{\text{Moon}} = 87\% \pm 10\%$  in this paper.

We used an SIS mixer receiver with noise temperature of  $T_{\text{rx}} \sim 900$  K in a single sideband mode realized by a quasi-optical Martin-Pupplet-type filter in front of the feed horn (Manabe et al. 2003). The slightly high receiver noise temperature results from the higher physical temperature of the mixer and image signal terminating load due to the limited cooling capability of a compact cryocooler. The sideband rejection ratio was measured to be  $21 \pm 4$  dB at 461 GHz. The typical system noise temperature including the atmospheric effect was 2500–4000 K at the observing elevations. The receiver backend was an FX-type digital spectrometer with 16384 channels, with a total bandwidth and frequency resolution of 1 GHz and 61 kHz, corresponding to  $650 \text{ km s}^{-1}$  and  $0.04 \text{ km s}^{-1}$ , respectively, at

461 GHz. A band-pass filter was inserted in front of the spectrometer to avoid the aliasing effect, so the effective bandwidth of the spectrometer was 40–960 MHz, covering  $600 \text{ km s}^{-1}$  in velocity. We observed 685 positions in the region of  $7.125 \text{ deg}^2$  on the sky (figure 1). All observations were carried out in position-switching mode, with a selected reference position of  $(\alpha_{J2000.0}, \delta_{J2000.0}) = (05^{\text{h}}32^{\text{m}}12^{\text{s}}.7, -6^{\circ}27'53''.4)$  adopted from the CO ( $J=3-2$ ) mapping with the Mt. Fuji submillimeter-wave telescope (Ikeda et al. 1999). The observed positions were spaced every  $7.5$  in the equatorial coordinate. Additional data around Orion KL were obtained with a grid spacing of  $3/75$ .

The pointing of the telescope was checked by observing bright stars using an optical CCD camera mounted on a stay of the subreflector. In addition, we observed CO ( $J=4-3$ ) of Orion KL several times a day with a nine-point cross scan of  $4.5$  spacing in order to check variations of the pointing and intensity scale. Measured pointing accuracy was always better than  $1'$ , corresponding to about one tenth of the beam size. The calibration of the line intensity was made using a black body at ambient temperature by the standard chopper-wheel method (Penzias & Burrus 1973; Ulich & Haas 1976) every 15 minutes or more often, yielding an antenna temperature,  $T_{\text{A}}^*$ , corrected for atmospheric and antenna ohmic losses. Relative intensity variations of Orion KL were within 10% in rms. In this paper, we use as the intensity scale the main-beam brightness temperature, defined by  $T_{\text{mb}} = T_{\text{A}}^* / \eta_{\text{mb}}$ .

We achieved an rms noise level of  $\Delta T_{\text{mb}} = 0.5$  K at a resolution of  $0.6 \text{ km s}^{-1}$  for the CO ( $J=4-3$ ) line data

**Table 1.** Summary of  $^{12}\text{CO}$  ( $J=4-3$ ) observations with the Tsukuba 30 cm telescope.

Telescope	
Antenna diameter	30 cm
Angular resolution (HPBW)	$9.4 \pm 0.4$
Main beam efficiency	$0.87 \pm 0.10$
Receiver noise temperature	900 K
Sideband rejection ratio	$21 \pm 4$ dB
Bandwidth of spectrometer	40–960 MHz ( $\pm 300 \text{ km s}^{-1}$ at 461 GHz)
Resolution of spectrometer	61 kHz ( $0.04 \text{ km s}^{-1}$ at 461 GHz)
Site	
Place	Parinacota, Chile
Location	$18^\circ 12' \text{ S}, 69^\circ 16' \text{ W}$
Altitude	4400 m
Observations	
Date	2011 September 15–October 17
Rest frequency of $^{12}\text{CO}$ ( $J=4-3$ )	461.04077 GHz
System noise temperature	2500–4000 K
Pointing accuracy	$< 1.0$
Observing area	$7.125 \text{ deg}^2$
Numbers of positions	685
Grid spacing	$7.5$ ( $3/25$ around Orion KL)
Reference position	$(\alpha_{\text{J2000.0}}, \delta_{\text{J2000.0}}) = (05^{\text{h}}32^{\text{m}}12^{\text{s}}.7, -6^\circ 27' 53'')$
Noise level in $T_{\text{mb}}$ scale	$0.5 \text{ K}$ with smoothing velocity of $0.6 \text{ km s}^{-1}$

after integrating typically 5 minutes per position. We reduced the data using the NEWSTAR package, which is reduction software developed by the Nobeyama Radio Observatory. The reduction procedure included flagging bad data, integrating the data, and removing a slope in the base line by least-squares fitting of the first-order polynomial. The details of the observations are summarized in table 1.

### 3 Results

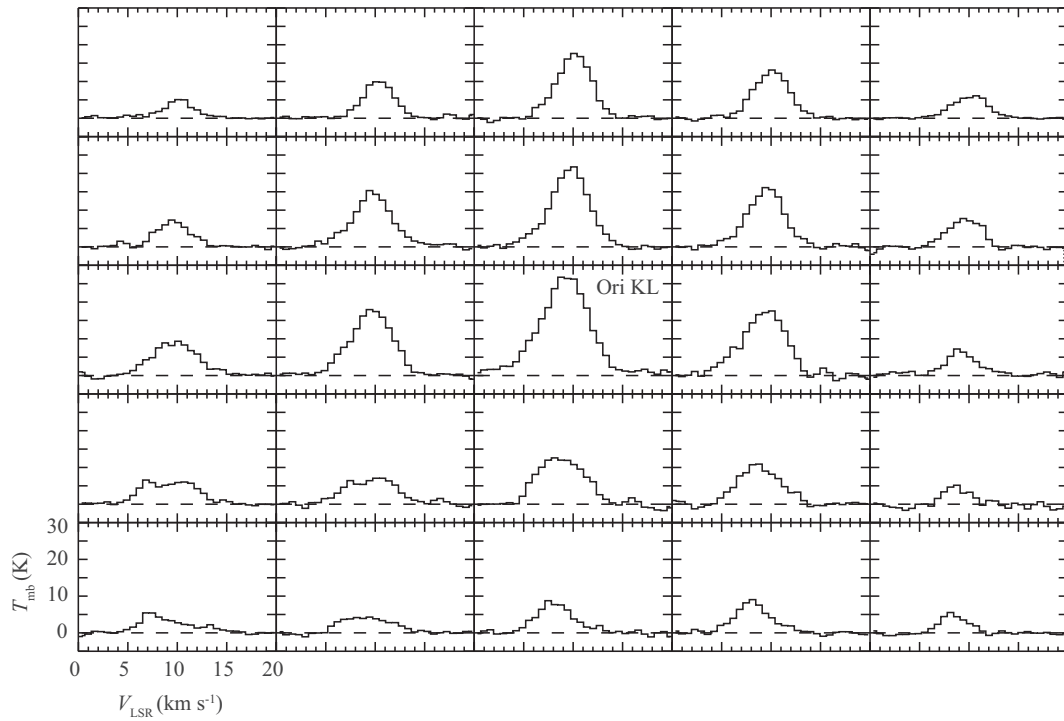
Figure 3 shows samples of the  $\text{CO}$  ( $J=4-3$ ) spectra measured around Orion KL. Figure 4a shows the intensity map of  $\text{CO}$  ( $J=4-3$ ) integrated over the velocity range of  $V_{\text{LSR}} = 0-20 \text{ km s}^{-1}$ ,  $I_{\text{CO}} = \int T_{\text{mb}} dv$ . The map indicates an elongated cloud north to south with a length of  $\sim 30 \text{ pc}$  ( $4.2'$ ) and width of  $\sim 6 \text{ pc}$  ( $50''$ ). The strongest emissions appear at the position of Orion KL with a peak temperature of  $T_{\text{mb}} = 26.8 \text{ K}$ , an integrated intensity of  $I_{\text{CO}} = 168.4 \text{ K km s}^{-1}$ , a line width of  $\Delta V = 5.4 \text{ km s}^{-1}$ , and a peak velocity of  $V_{\text{LSR}} = 9.5 \text{ km s}^{-1}$ . The obtained intensity and peak velocity are compared with previous observations by Schulz et al. (1995) after correcting an effect due to the difference in the angular resolutions of the telescopes, and are consistent within the calibration error (for details, see Ishii et al. 2013).

In the southern part of Orion A, bright and faint  $\text{CO}$  ( $J=4-3$ ) regions are seen at L1641-N ( $\alpha_{\text{J2000.0}}, \delta_{\text{J2000.0}} = 05^{\text{h}}36^{\text{m}}19^{\text{s}}.0, -6^\circ 22' 13.3''$ ), L1641-S2 ( $05^{\text{h}}42^{\text{m}}47^{\text{s}}.2, -8^\circ 17' 5.5''$ ), and L1641-S4 ( $05^{\text{h}}40^{\text{m}}48^{\text{s}}.8, -8^\circ 06' 50.9''$ ), which are known as molecular outflows associated with the star-forming region(s) of low-/intermediate-mass stars (Fukui 1989). Figure 4b shows the peak brightness temperature map. Another peak is also located at ( $05^{\text{h}}38^{\text{m}}0^{\text{s}}.0, -7^\circ 05' 00''$ ), at the west of L1641-Center ( $05^{\text{h}}38^{\text{m}}46^{\text{s}}.4, -7^\circ 01' 5.0''$ ), also identified in  $\text{CO}$  ( $J=1-0$ ).

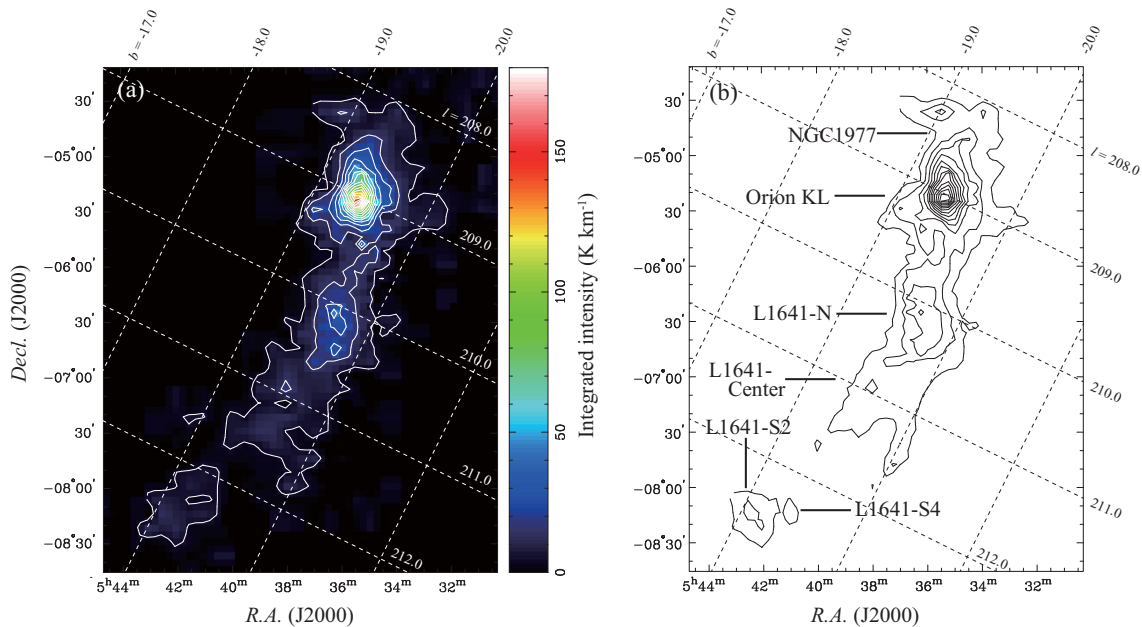
In the north of Orion A, a peak near NGC 1977 at ( $05^{\text{h}}35^{\text{m}}30^{\text{s}}, -4^\circ 35' 00''$ ) is manifested only in the peak temperature map of  $\text{CO}$  ( $J=4-3$ ). The  $\text{CO}$  emission decreases steeply in both the temperature and the integrated intensity maps, to the northeastern Orion KL. This is consistent with the results of the previous observations in  $^{12}\text{CO}$  ( $J=1-0$ ) and  $^{13}\text{CO}$  ( $J=1-0$ ) (Bally et al. 1987; Wilson et al. 2005). In addition, the east edge of L1641-N also shows a steep change in the peak temperature map, with the emission from the gas component extending toward the southwest direction of L1641-N.

Figure 5a shows the temperature-weighted mean velocity (first moment map) defined by  $\int T_{\text{mb}} v dv / \int T_{\text{mb}} dv$ . The  $\text{CO}$  ( $J=4-3$ ) profiles show velocity components beyond  $14 \text{ km s}^{-1}$  around H II regions, M42 (Orion KL) and NGC 1977 (e.g., figure 3), as seen in  $^{12}\text{CO}$  ( $J=1-0$ ) but not in  $^{13}\text{CO}$  ( $J=1-0$ ) or in [C I] (Bally et al. 1987;





**Fig. 3.** Samples of the CO ( $J=4-3$ ) spectra measured around Orion KL, parallel to the right ascension and declination. For each spectrum, the abscissa is the LSR velocity ( $V_{\text{LSR}}=0-20 \text{ km s}^{-1}$ ) and the ordinate is the main-beam brightness temperature ( $T_{\text{mb}}=-5-30 \text{ K}$ ). The grid spacing between the spectra is  $7''.5$ .



**Fig. 4.** (a) Integrated intensity map of  $^{12}\text{CO}(J=4-3)$ . The contour levels are from  $I_{\text{CO}}=5 \text{ K km s}^{-1}$  to  $165 \text{ K km s}^{-1}$  with an interval of  $10 \text{ K km s}^{-1}$ . (b) Peak main-brightness temperature map of  $^{12}\text{CO}(J=4-3)$ . The contour levels are from  $T_{\text{mb}}=2 \text{ K}$  to  $26 \text{ K}$  with an interval of  $2 \text{ K}$ .

Nagahama et al. 1998; Ikeda et al. 2002). In the southern region, from  $\text{Dec} = -7^\circ 30'$  to  $\text{Dec} = -6^\circ 45'$ , the mean velocity at the east side of the clouds was  $2-3 \text{ km s}^{-1}$  lower than that at the west side. Figure 5b shows a line width map calculated from the second-order moment map. The large

velocity width of  $\Delta V > 4 \text{ km s}^{-1}$  is distributed in the region within  $\sim 15'$  of the Orion KL center. The broad velocity width of  $3 \text{ km s}^{-1}$  is also detected at the east side of L1641-N and at the CO integrated intensity peak of L1641-S4. The broad CO emission at L1641-S4 corresponds to a

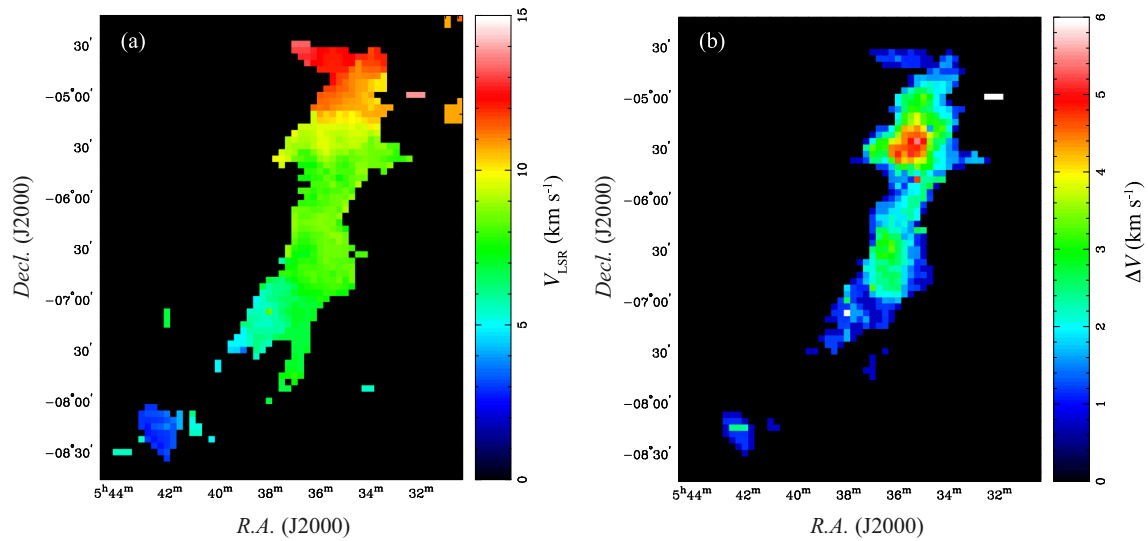


Fig. 5. Maps of spatial distribution of (a) temperature-weighted velocity and (b) velocity width (FWHM) of  $^{12}\text{CO}$  ( $J=4-3$ ) in the region of  $T_{\text{mb}} > 2.0$  K.

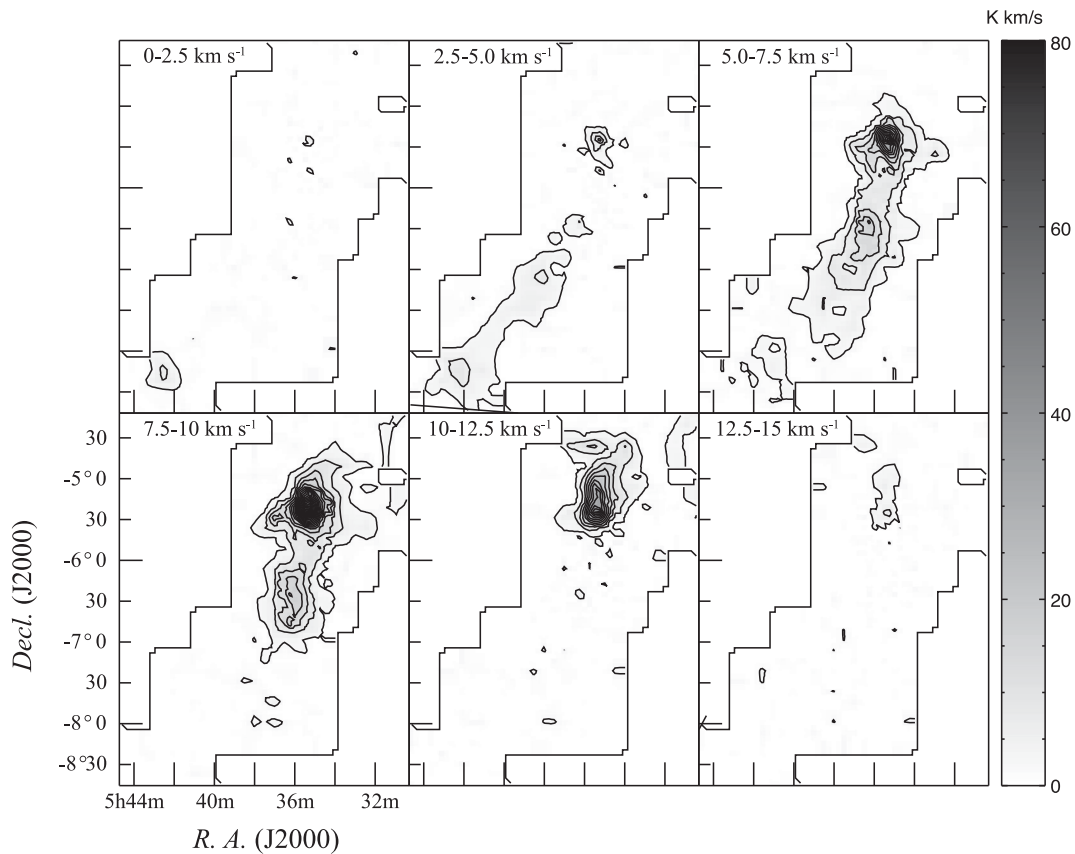
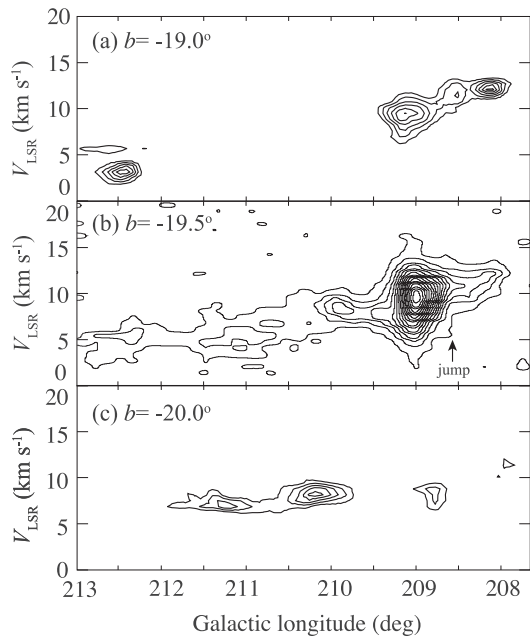


Fig. 6. Channel map of  $^{12}\text{CO}$  ( $J=4-3$ ). The velocity ranges are indicated at the top left corner of each map. The contour levels are from  $2 \text{ K km s}^{-1}$  to  $80 \text{ K km s}^{-1}$  with an interval of  $4 \text{ K km s}^{-1}$ .

component in channel maps of  $0-2.5$  and  $2.5-5.0 \text{ km s}^{-1}$  (figure 6). The high velocity component on the north has a small velocity width of  $1.7 \text{ km s}^{-1}$ .

Figure 7 shows position-velocity diagrams along the galactic longitude at  $b = -19^{\circ}0'$ ,  $b = -19^{\circ}5'$ , and

$b = -20^{\circ}0'$ . It shows the velocity gradient from 2 to  $14 \text{ km s}^{-1}$  along the center of the cloud as noticed in the temperature-weighted velocity map. The  $\text{CO}$  ( $J=1-0$ ) emission has a velocity jump at  $l \sim 208^{\circ}5'$  in the position-velocity diagram (figure 5b in Wilson et al. 2005), where there is



**Fig. 7.** Longitude-velocity diagram of  $^{12}\text{CO}$  ( $J=4-3$ ) at (a)  $b = -19.0^\circ$ , (b)  $b = -19.5^\circ$ , and (c)  $b = -20.0^\circ$ . The contour levels are from  $T_{\text{mb}} = 2\text{ K}$  with an interval of 1 K.

no low velocity component ( $\leq 5\text{ km s}^{-1}$ ) beyond the jump point. This suggests that the low velocity molecular gas has been cleared at  $l < 208.5$ . The same velocity jump was detected in the CO ( $J=4-3$ ) at  $l \approx 208.75$  (figure 7b). It forms a CO edge at  $l = 210.0$ , and there is no CO ( $J=4-3$ ) at  $V_{\text{LSR}} < 8\text{ km s}^{-1}$  at  $l < 208.5$ . Figure 6 also represents this trend. The filamentary structure has low ( $\sim 6\text{ km s}^{-1}$ ) and high velocity ( $\sim 12\text{ km s}^{-1}$ ) components at the west side of Orion KL. L1641-S4 has wide velocities of  $1.5\text{ km s}^{-1}$  to  $7\text{ km s}^{-1}$ .

## 4 Discussion

We derive the physical conditions of the molecular gas in the Orion-A GMC by a non-LTE analysis, combining our  $^{12}\text{CO}$  ( $J=4-3$ ) data and archival data,  $^{12}\text{CO}$  ( $J=1-0$ ) and  $^{13}\text{CO}$  ( $J=1-0$ ). The  $^{12}\text{CO}$  ( $J=1-0$ ) data are a part of the Columbia survey (Dame et al. 2001; Wilson et al. 2005). The survey mapped the region of Orion A with a spatial resolution of  $8''.4$  and a grid spacing of  $0''.125$  in the galactic coordinates. The velocity resolution is  $0.65\text{ km s}^{-1}$ , the same as  $^{12}\text{CO}$  ( $J=4-3$ ). The typical rms noise level is  $\Delta T_{\text{mb}} = 0.26\text{ K}$ .

For  $^{13}\text{CO}$  ( $J=1-0$ ), the data taken with the Bell 7 m telescope (Bally et al. 1987) are adopted, where the beam size was  $\text{HPBW} = 1''.8$ . The data consisted of 33000 positions in the region of  $8\text{ deg}^2$  with a grid spacing of  $1'$ . Spectra covered from  $V_{\text{LSR}} = 1.0$  to  $14\text{ km s}^{-1}$  with a velocity resolution of  $0.27\text{ km s}^{-1}$ . The noise level was  $\Delta T_{\text{mb}} = 0.30\text{ K}$ .

### 4.1 Integrated intensity maps

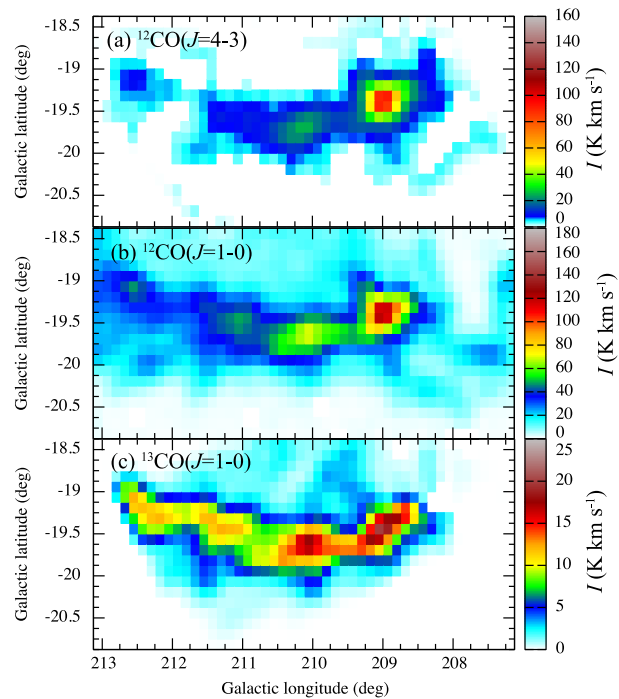
The data grid of the  $^{12}\text{CO}$  ( $J=4-3$ ) and  $^{13}\text{CO}$  ( $J=1-0$ ) maps were converted from the equatorial coordinates to the galactic coordinates to be coincident with the  $^{12}\text{CO}$  ( $J=1-0$ ) map, at the observing positions. We also convolved the  $^{13}\text{CO}$  ( $J=1-0$ ) data with a Gaussian function to yield the angular resolution of  $\text{FWHM} = 9''.44$ , the same as that of the  $^{12}\text{CO}$  ( $J=4-3$ ).

We calculated the intensity of each line integrated from  $1.0\text{ km s}^{-1}$  to  $14.0\text{ km s}^{-1}$ ,  $I_{^{12}\text{CO}(4-3)}$ ,  $I_{^{12}\text{CO}(1-0)}$ , and  $I_{^{13}\text{CO}(1-0)}$ , for the analysis. As mentioned above, a small fraction of the molecular gas associated with Orion KL has a velocity  $V_{\text{LSR}} > 14\text{ km s}^{-1}$ , but the effect of the higher velocity gas on the present analysis is negligible. Averages of the integrated intensities are  $I_{^{12}\text{CO}(4-3)} = 14.6$ ,  $I_{^{12}\text{CO}(1-0)} = 58.8$ , and  $I_{^{13}\text{CO}(1-0)} = 8.3\text{ K km s}^{-1}$  in the mapped region. The rms uncertainty of the integrated intensity at each position is described as

$$\Delta I = \Delta T \sqrt{\Delta V \Delta V_s}, \quad (1)$$

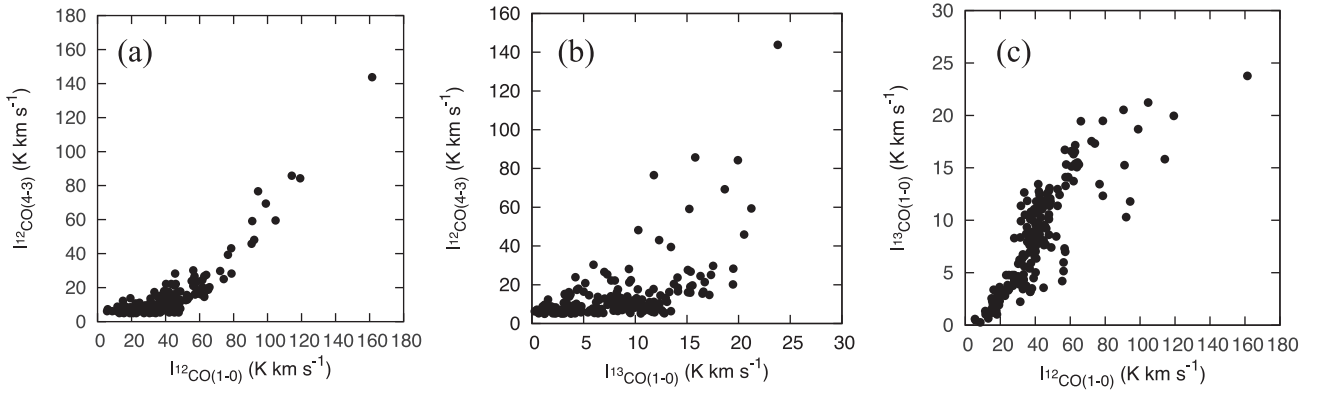
where  $\Delta T$  is the rms noise,  $\Delta V$  the velocity width of a spectrum, and  $\Delta V_s$  the smoothed velocity resolution. Typical values of  $\Delta I$  for  $I_{^{12}\text{CO}(4-3)}$ ,  $I_{^{12}\text{CO}(1-0)}$ , and  $I_{^{13}\text{CO}(1-0)}$  are 0.5, 0.9, 0.4  $\text{K km s}^{-1}$ , respectively, for the average line width of the three lines,  $\Delta V = 5.0\text{ km s}^{-1}$ .

Figure 8 shows the integrated intensity map of the three lines. The integrated intensity map of CO ( $J=4-3$ )



**Fig. 8.** Integrated intensity map of (a)  $^{12}\text{CO}$  ( $J=4-3$ ), (b)  $^{12}\text{CO}$  ( $J=1-0$ ), and (c)  $^{13}\text{CO}$  ( $J=1-0$ ), where the data of  $^{12}\text{CO}$  ( $J=1-0$ ) and  $^{13}\text{CO}$  ( $J=1-0$ ) were adopted from Wilson et al. (2005) and Bally et al. (1987).





**Fig. 9.** Correlation of the integrated intensities between (a)  $I_{12\text{CO}(1-0)}$  and  $I_{12\text{CO}(4-3)}$ , (b)  $I_{13\text{CO}(1-0)}$  and  $I_{12\text{CO}(4-3)}$ , and (c)  $I_{12\text{CO}(1-0)}$  and  $I_{13\text{CO}(1-0)}$ , where the data of  $^{12}\text{CO}(1-0)$  and  $^{13}\text{CO}(1-0)$  were adopted from Wilson et al. (2005) and Bally et al. (1987).

emission exhibits smaller spatial distribution than those of  $\text{CO}(J=1-0)$  and  $\text{CO}(J=2-1)$  emissions (Wilson et al. 2005; Sakamoto et al. 1994) despite similar noise levels. Figure 9 shows correlation plots between the integrated intensities of the three lines. Figure 9a indicates a good correlation between  $I_{12\text{CO}(4-3)}$  and  $I_{12\text{CO}(1-0)}$  at  $I_{12\text{CO}(1-0)} > 60 \text{ K km s}^{-1}$ , but  $I_{12\text{CO}(4-3)}$  is weak at  $I_{12\text{CO}(1-0)} < 40 \text{ K km s}^{-1}$ . CO molecules are not populated well for the density corresponding to  $I_{12\text{CO}(1-0)} < 40 \text{ K km s}^{-1}$ . The correlation of  $I_{12\text{CO}(4-3)}$  with  $I_{13\text{CO}(1-0)}$  can be seen in figure 9b, but the dispersion of the scatter plot is larger than that with the dispersion of  $I_{12\text{CO}(1-0)}$ . The  $I_{13\text{CO}(1-0)} - I_{12\text{CO}(1-0)}$  plot in figure 9c has comparable dispersion. As in the case with the  $I_{12\text{CO}(1-0)}$  plot,  $I_{12\text{CO}(4-3)}$  is weak for  $I_{13\text{CO}(1-0)} < 15 \text{ K km s}^{-1}$ .

## 4.2 Non-LTE analysis

### 4.2.1 Correlation between the intensities of $\text{CO}(4-3)$ and lower CO transitions

Intensity ratios can be used to probe the rough trend of the physical conditions of the molecular gas. We define beam-averaged intensity ratios between  $^{12}\text{CO}(J=4-3)$ ,  $^{12}\text{CO}(J=1-0)$ , and  $^{13}\text{CO}(J=1-0)$ ,

$$r_{4-3/1-0} = I_{12\text{CO}(4-3)} / I_{12\text{CO}(1-0)}, \quad (2)$$

$$r_{4-3/13} = I_{12\text{CO}(4-3)} / I_{13\text{CO}(1-0)}, \quad (3)$$

$$r_{13/12} = I_{13\text{CO}(1-0)} / I_{12\text{CO}(1-0)}, \quad (4)$$

where the beam sizes for the lines are almost the same. Typical uncertainties of  $r_{4-3/1-0}$ ,  $r_{4-3/13}$ , and  $r_{13/12}$  are  $\Delta r_{4-3/1-0} = 0.02$ ,  $\Delta r_{4-3/13} = 0.03$ , and  $\Delta r_{13/12} = 0.01$ , respectively.

Figure 10 shows the spatial distributions of the intensity ratios. Denser and warmer hydrogen can populate the CO

molecules to higher excitation levels and produce higher rotational transition emission such as  $\text{CO}(J=4-3)$ . Thus  $r_{4-3/1-0}$  would be high at the regions where the dense and/or warm gas is associated.  $r_{4-3/13}$  and  $r_{13/12}$  would be also emphasized the distributions of the warm gas and dense gas, respectively. We examine the trend of the physical conditions of the molecular gas using the ratio maps (figure 10), which will be compared with the results of the RADEX calculations in the next subsection. There are two peaks of  $r_{4-3/1-0}$  (figure 10a). One with  $r_{4-3/1-0} = 0.9 \pm 0.2$  at

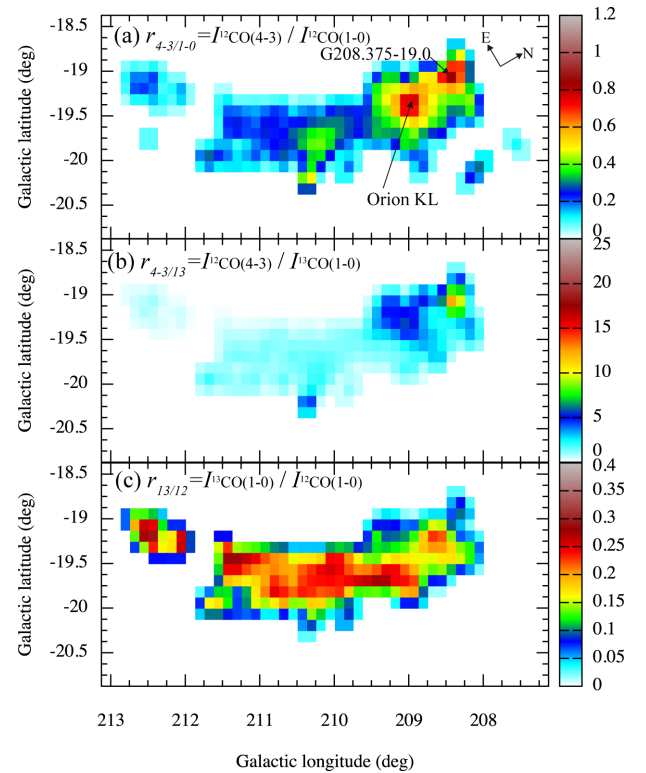


**Fig. 10.** Distributions of the intensity ratios of (a)  $r_{4-3/1-0}$ , (b)  $r_{4-3/13}$ , and (c)  $r_{13/12}$ , where the data of  $^{12}\text{CO}(J=1-0)$  and  $^{13}\text{CO}(J=1-0)$  were adopted from Wilson et al. (2005) and Bally et al. (1987).

$(l, b) \approx (209^\circ, -19^\circ 37')$  corresponds to Orion KL, which is the most active star-forming region in the Orion-A GMC and is also identified in the integrated intensity map. The other (we refer to it as G208.375–19.0), with  $r_{4-3/1-0} = 1.1 \pm 0.3$ , is at  $(l, b) \approx (208^\circ 37', -19^\circ)$ , the north of Orion KL. This peak is identified in the ratio map only. In addition, it seems that the relatively high ratio ( $r_{4-3/1-0} > 0.5$ ) traces the “CO front,” which is a region having a sharp contrast, at the eastern edge of the main component of Orion A (OMC-2/3), that is shown in a high resolution mapping of Orion A in the CO ( $J=1-0$ ) line by Shimajiri et al. (2011). Nishimura et al. (2015) also reported a high  $^{12}\text{CO}$  ( $J=2-1$ )/ $^{12}\text{CO}$  ( $J=1-0$ ) ratio around G208.375–19.0, while the high  $r_{4-3/1-0}$  clearly shows a peak value of 1.1 just at G208.375–19.0. Their  $^{13}\text{CO}$  ( $J=2-1$ )/ $^{12}\text{CO}$  ( $J=2-1$ ) map shows maxima toward G208.375–19.0, which may trace the same gas highlighted by  $r_{4-3/1-0}$ .

As mentioned in the introduction, some studies speculated that the diffuse gas is swept up by Orion OB associations and collided with Orion A. This may cause the heating of the gas. We note that the star cluster NGC 1977 contains a B star, HD 37018, and may be an alternative heating source of the gas around G208.375–19.0, where  $r_{4-3/1-0}$  shows  $1.1 \pm 0.3$ . G208.375–19.0 shows a high ratio of  $r_{4-3/13} > 10$ , while  $r_{13/12}$  is moderate,  $\sim 0.1$ . In the Gaussian fit of spectra of CO ( $J=4-3$ ), CO ( $J=1-0$ ),  $^{13}\text{CO}$  ( $J=1-0$ ) at G208.375–19.0, the peak velocity and the line width (FWHM) are measured to be  $V_{\text{LSR}} = 12.1 \pm 0.7$ ,  $12.1 \pm 0.7$ , and  $12.2 \pm 0.3 \text{ km s}^{-1}$  and  $\Delta V = 1.6$ ,  $1.5$ , and  $1.0 \text{ km s}^{-1}$ , respectively. This high-ratio region extends like a filament that traces the CO front. Orion KL also shows the high ratio of  $r_{4-3/13} \sim 5$ , but the ratio is less than that for G208.375–19.0. Further, the  $I_{^{13}\text{CO}(1-0)}/I_{^{12}\text{CO}(1-0)}$  map (figure 10c) shows the high ratio at the southern ( $l < 209^\circ$ ) side of Orion A. A peak of  $r_{13/12}$  can be found at the inside of G208.375–19.0 near the CO front. This would reflect that the density of the gas is increasing at the inside of the CO front. Near L1641-N at  $(l, b) \approx (210^\circ 12', -19^\circ 75')$ ,  $r_{4-3/1-0} = 0.45$  is higher than the entire average, but the distribution of the high  $r_{13/12}$  ( $= 0.23\text{--}0.3$ ) region is wider than that of  $r_{4-3/1-0}$  and has an offset from L1641-N toward the northeast direction.

#### 4.2.2 RADEX calculation

We adopted RADEX (van der Tak et al. 2007) to estimate the physical conditions of the molecular gas in Orion A. RADEX is a non-LTE radiative transfer computer code. Using RADEX, we calculated the intensity ratios for given physical parameters of the molecular

gas, the kinetic temperature  $T_{\text{kin}}$ , the density of molecular hydrogen  $n(\text{H}_2)$ , and the column density of  $^{12}\text{CO}$  per unit velocity width of the spectrum  $N(^{12}\text{CO})/dV$ . The ranges of individual input parameters were  $T_{\text{kin}} = 5\text{--}100 \text{ K}$ ,  $n(\text{H}_2) = 10\text{--}10^8 \text{ cm}^{-3}$ , and  $N(^{12}\text{CO})/dV = 10^{13}\text{--}10^{19} \text{ cm}^{-2} (\text{km s}^{-1})^{-1}$ . We assumed the typical line width of the spectra as  $dV = 5.0 \text{ km s}^{-1}$  from observations and adopted a  $[^{12}\text{CO}]/[^{13}\text{CO}]$  abundance ratio of 50 and a background temperature of 2.73 K. The assumed line width would be larger than that in the peripheral region ( $dV \approx 2\text{--}3 \text{ km s}^{-1}$ ). However, the calculation of physical parameters,  $T_{\text{kin}}$ ,  $n(\text{H}_2)$ , and  $N(^{12}\text{CO})/dV$  is independent of the line width as long as we use the ratio of the integrated intensities. It is to be noted that the difference in the line width should be taken into account when we estimate the column density  $N(^{12}\text{CO})$  from  $N(^{12}\text{CO})/dV$ . We assumed that the geometry and density structures of the molecular gas follow the standard homogenous-sphere model for the escape probability of photons in RADEX calculations. Only  $\text{H}_2$  was taken into account as the collision partner with CO molecules. The collisional coefficients between  $\text{H}_2$  molecules and  $^{12}\text{CO}/^{13}\text{CO}$  were taken from the Leiden Atomic and Molecular Database (LAMDA: Schöier et al. 2005). RADEX returned the integrated intensities of  $^{12}\text{CO}$  ( $J=4-3$ ),  $^{12}\text{CO}$  ( $J=1-0$ ), and  $^{13}\text{CO}$  ( $J=1-0$ ) using the given physical parameters of  $T_{\text{kin}}$ ,  $n(\text{H}_2)$ , and  $N(^{12}\text{CO})/dV$ .

$\chi^2$  was evaluated to estimate the physical parameters from the results of the RADEX calculation, using

$$\begin{aligned} \chi^2 = & [r_{4-3/1-0} - R_{4-3/1-0}(T, n, N/dV)]^2 \\ & + [r_{4-3/13} - R_{4-3/13}(T, n, N/dV)]^2 \\ & + [r_{13/12} - R_{13/12}(T, n, N/dV)]^2, \end{aligned} \quad (5)$$

where  $R_{4-3/1-0}$ ,  $R_{4-3/13}$ , and  $R_{13/12}$  are the calculated intensity ratios using RADEX results and are functions of  $T_{\text{kin}}$ ,  $n$ , and  $dN/dV$ . A set of physical conditions was found as the best combination of  $T_{\text{kin}}$ ,  $n_{\text{H}_2}$ , and  $N(^{12}\text{CO})/dV$  which minimized the  $\chi^2$  value. The average of the minimized  $\chi^2$  was  $3.6 \times 10^{-4}$ , which corresponds to a deviation between the observed and calculated ratios of 0.01, which is comparable with the rms of each intensity ratio.

#### 4.3 Spatial distribution of the physical conditions

Figure 11 shows the distribution of the three output parameters of  $T_{\text{kin}}$ ,  $n_{\text{H}_2}$ , and  $N(^{12}\text{CO})/dV$ , calculated by RADEX, overlaid on an extinction map made with 2MASS data (Dobashi 2011). The kinetic temperature and the density toward Orion KL are  $T_{\text{kin}} = 80\text{--}100 \text{ K}$  and  $n_{\text{H}_2} \sim 10^5 \text{ cm}^{-3}$ , respectively. These values are consistent with the results

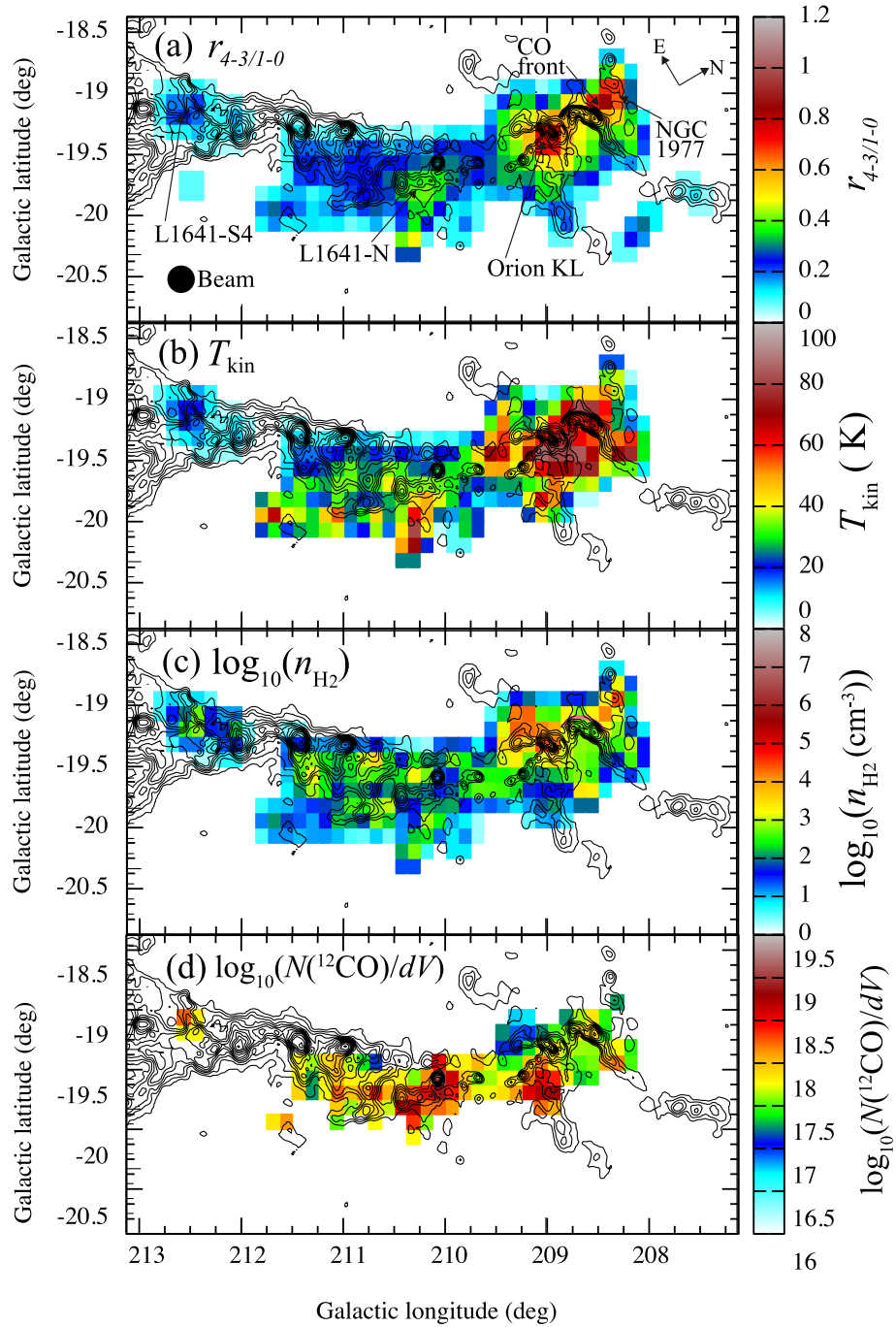


**Fig. 11.** Distribution of (a)  $r_{4-3/1-0} = I_{12\text{CO}(4-3)} / I_{12\text{CO}(1-0)}$ , (b) the kinetic temperature  $T_{\text{kin}}$ , (c) the volume number density of  $n_{\text{H}_2}$ , and (d)  $N(^{12}\text{CO})/dV$  in color. The contour map shows extinction estimated from the 2MASS data (Dobashi 2011).

estimated so far (Schulz et al. 1995). The column density per unit velocity is  $N(^{12}\text{CO})/dV \sim 10^{18} \text{ cm}^{-2} (\text{km s}^{-1})^{-1}$ . Although the number density at the west side of Orion KL decreases with the distance from Orion KL, the number density at the east side of Orion KL shows a relatively high value ( $\sim 10^4 \text{ cm}^{-3}$ ). In contrast, the column density  $N(^{12}\text{CO})/dV$  is high at the west side and low at the east

side, indicating that the optical depth at the west is high and that at the east is low.

The physical parameters at G208.375–19.0 are  $T_{\text{kin}} \sim 80 \text{ K}$  and  $n_{\text{H}_2} \sim 10^4\text{--}10^5 \text{ cm}^{-3}$ . The warm temperature region of  $T_{\text{kin}} \sim 60 \text{ K}$  around G208.375–19.0 extends toward the CO front that is traced as a filamentary structure in the extinction map. The high density region, with

$n_{\text{H}_2} \sim 10^4 \text{ cm}^{-3}$ , may be localized at the northeast of the CO front near NGC 1977 at  $(l, b) = (208^\circ.5, -19^\circ.1)$  (Peterson & Megeath 2008). However, the angular resolution ( $9''.4$ ) of the 30 cm telescope is insufficient to determine the accurate position of G208.375–19.0. The column density is  $10^{17}\text{--}10^{18} \text{ cm}^{-2} (\text{km s}^{-1})^{-1}$  at G208.375–19.0, which is comparable with that of Orion KL. There is no clear difference in the density and column density at the east and west sides of G208.375–19.0.

The warm gas of  $\sim 40 \text{ K}$  is associated with L1641-N. The density is not so high,  $\sim 10^3 \text{ cm}^{-3}$ , around L1641-N, but the column density of  $^{12}\text{CO}$  is high,  $\sim 10^{18} \text{ cm}^{-2} (\text{km s}^{-1})^{-1}$ . This indicates that the optical depth in L1641-N is larger than that of the gas at the northern part of the Orion-A GMC. In L1641-S4, the temperature and the density are less than  $20 \text{ K}$  and  $\sim 10^3 \text{ cm}^{-3}$ , respectively. Several local parts of L1641-S4 show a column density of  $\sim 10^{18} \text{ cm}^{-2} (\text{km s}^{-1})^{-1}$ . This is less than that of L1641-N, but higher than that for the northern part of the Orion-A GMC.

The Orion-A GMC has a global gradient of the physical properties. The temperature decreases from north ( $\sim 100 \text{ K}$ ) to south ( $\sim 20 \text{ K}$ ), which is basically consistent with the results derived by CO ( $J=2-1$ ) and  $^{12}\text{CO}$  ( $J=1-0$ ) emissions (Nishimura et al. 2015). Moreover, the temperature is lower at the east side than the west side in the southern part of the Orion-A GMC. The density distribution shows an almost constant value of  $\sim 10^3 \text{ cm}^{-3}$ , except for the gas associated with Orion KL and the CO front. The column density per unit velocity of  $^{12}\text{CO}$  has a gradient along the north–south direction. The column density increases from the northern part [ $\sim 10^{17.5} \text{ cm}^{-2} (\text{km s}^{-1})^{-1}$ ] to the southern part [ $\sim 10^{18-19} \text{ cm}^{-2} (\text{km s}^{-1})^{-1}$ ] where the L1641-N region is included. Medians of  $T_{\text{kin}}$ ,  $n_{\text{H}_2}$ , and  $N(^{12}\text{CO})/dV$  in the entire observed region of figure 11 are  $34 \text{ K}$ ,  $3.5 \times 10^2 \text{ cm}^{-3}$ , and  $5.3 \times 10^{17} \text{ cm}^{-2} (\text{km s}^{-1})^{-1}$ , respectively. This median of the density is consistent with that reported by Sakamoto et al. (1994).

#### 4.4 Physical property and triggered star formation

G208.375–19.0 contains warm and dense gas and associates with the CO front. Recently, several large telescopes have started to survey the Orion-A GMC with higher angular resolution, mainly focused on the detailed structure of the GMC such as filaments, clumps, cores, and outflows in particular parts of the cloud. Shimajiri et al. (2011) clearly showed that the diffuse CO component is interacting with the CO front and is being accumulated onto the

surface of the main cloud component at the CO front (figure 14 in Shimajiri et al. 2011). Some authors suggested that the Orion OB 1a or 1b group, located  $\sim 100 \text{ pc}$  east from the Orion-A GMC, affected Orion-A by its strong UV emission ( $G_0 = 10^{4-5}$ ) and stellar wind (Tielens & Hollenbach 1985; Bally et al. 1987; Wilson et al. 2005). The radiation pressure of these OB stars may sweep up the pre-existing diffuse gas toward Orion A and trigger the next star formation episode in the cloud (e.g., Elmegreen & Lada 1977). Similarly, G208.375–19.0 would be interpreted as the result of the heating and accumulating of the diffuse material affected by the Orion OB association. G208.375–19.0 is also close to NGC 1977 and may be affected by B stars in NGC 1977, alternatively. Unfortunately, the low angular resolution of the 30 cm telescope cannot determine the spatial relation of G208.375–19.0 and the CO front or NGC 1977. Observations with higher resolution are needed to confirm the origin of the high ratio at G208.375–19.0.

## 5 Conclusion

The  $^{12}\text{CO}$  ( $J=4-3$ ) line emission in the Orion-A GMC has been mapped with a  $9''.4 \pm 0''.4$  resolution using the Tsukuba 30 cm telescope. We investigated the physical properties of the molecular gas over the clouds. The conclusions are summarized as follows:

- (1) The emission of CO ( $J=4-3$ ) extends over  $3 \text{ deg}^2$  with  $T_{\text{mb}} > 2.0 \text{ K}$ , covering the main component of the molecular gas in the Orion-A GMC. The most intense emission of  $T_{\text{mb}} = 27 \text{ K}$  was detected toward the Orion KL region. The other star-forming region, L1641-N, also has a peak in the integrated intensity map.
- (2) The velocity gradient from south to north of the main component of the GMC is observed in the same way for the  $^{12}\text{CO}$  ( $J=1-0$ ) and  $^{13}\text{CO}$  ( $J=1-0$ ) emission lines. A velocity jump at  $l \approx 208^\circ.5$  region is also traced in the longitude–velocity map.
- (3) The integrated intensity ratio between CO ( $J=4-3$ ) and CO ( $J=1-0$ ) is  $r_{4-3/1-0} \sim 0.2$  in the southern region and  $0.4\text{--}0.8$  at the star-forming regions of the cloud. Orion KL and a position near G208.375–19.0 on the CO front show maxima in the map of the ratio,  $0.9 \pm 0.2$  and  $1.1 \pm 0.3$ , respectively. G208.375–19.0 is clearly manifested for the first time in this  $r_{4-3/1-0}$  ratio map.
- (4) We derived physical properties of the molecular gas using non-LTE analysis. The kinetic temperature of the star-forming regions, Orion KL and L1641-N, are  $T_{\text{kin}} = 80\text{--}100 \text{ K}$  and  $40 \text{ K}$ , respectively. These results are consistent with the values estimated by previous

observations in lower transition lines of CO and its isotopologue. The results also indicate a gradient of the temperature that ranges within  $T_{\text{kin}} = 20$  K in the south to 80 K in the north.

- (5) The non-LTE analysis shows that the kinetic temperature and the density are increasing near the CO front including G208.375–19.0. The gas associated with the edge of the northeast part of the cloud including the CO front is warm ( $T_{\text{kin}} \sim 60$  K), dense ( $n_{\text{H}_2} \sim 10^4 \text{ cm}^{-3}$ ), and optically thin. This indicates the global compression of the gas in the northern part of Orion A. This may be caused by the heating by UV emission from OB stars or compressing of the gas by an accumulation of the diffuse gas to the CO front that relates with the triggered star formation. However, observations of the CO line from highly and moderately excited molecules with high angular resolution are needed to determine the location of the origin of this warm and dense gas.

## Acknowledgements

We are grateful to M. Ogino, Y. Ishizaki, M. Nakano, H. Okura, Y. Terabe, Y. Nihonmatsu, Y. Koide, D. Salak, K. Saito, K. Doihata, and N. Reyes for helping with the development of the 30 cm telescope and its operation. We would like to thank the referee, Ken'ichi Tatematsu, for his careful reading and constructive suggestions. We acknowledge the Corporación Nacional Forestal (CONAF) at Putre and people at Parinacota in Chile for their support during the operation of the telescope. The International Foundation High Altitude Research Stations Jungfraujoch and Gornergrat (HFSJG) made it possible for us to carry out the experiment at the station at Jungfraujoch in Switzerland. This work was supported by JSPS KAKENHI Grant Numbers 19204016, 22244011, and 26247019 and research grants of the Toray Science Foundation and the Mitsubishi Foundation. LB and RF gratefully acknowledge support by CONICYT Grant PFB-06, and FONDECYT projects 1120195 and 11140428.

## References

Bally, J., Lanber, W. D., Stark, A. A., & Wilson, R. W. 1987, *ApJ*, 312, L45  
 Bronfman, L., Cohen, R. S., Alvarez, H., May, J., & Thaddeus, P. 1988, *ApJ*, 324, 248  
 Brown, A. G. A., de Geus, E. J., & de Zeeuw, P. T. 1994, *A&A*, 289, 101  
 Dame, T. M., et al. 1987, *ApJ*, 322, 706  
 Dame, T. M., Hartmann, D., & Thaddeus, P. 2001, *ApJ*, 547, 792  
 Dobashi, K. 2011, *PASJ*, 63, S1

Dobashi, K., Bernard, J.-P., Yonekura, Y., & Fukui, Y. 1994, *ApJS*, 95, 419  
 Elmegreen, B. G., & Lada, C. J. 1977, *ApJ*, 214, 725  
 Fukui, Y. 1989, *ESO Conf. and Workshop Proc.*, 33, 95  
 Hirota, T., et al. 2007, *PASJ*, 59, 897  
 Ikeda, M., et al. 1999, *ApJ*, 527, L59  
 Ikeda, M., Oka, T., Tatematsu, K., Sekimoto, Y., & Yamamoto, S. 2002, *ApJS*, 139, 467  
 Ishii, S., et al. 2013, *IEEE Trans. Terahertz Science and Technology*, 3, 15  
 Johnstone, D., & Bally, J. 1999, *ApJ*, 510, L49  
 Johnstone, D., & Bally, J. 2006, *ApJ*, 653, 383  
 Kim, M. K., et al. 2008, *PASJ*, 60, 991  
 Kutner, M. L., Tucker, K. D., Chin, G., & Thaddeus, P. 1977, *ApJ*, 215, 521  
 Linsky, J. L. 1973, *Sol. Phys.*, 28, 409  
 Maddalena, R. J., Morris, M., Moscovitz, J., & Thaddeus, P. 1986, *ApJ*, 303, 375  
 Manabe, T., Inatani, J., Murk, A., Wylde, R., Seta, M., & Martin, D. H. 2003, *IEEE Trans. Microwave Theory and Techniques*, 51, 6  
 Menten, K. M., Reid, M. J., Forbrich, J., & Brunthaler, A. 2007, *A&A*, 474, 515  
 Mizuno, A., Onishi, T., Yonekura, Y., Nagahama, T., Ogawa, H., & Fukui, Y. 1994, *ApJ*, 445, L161  
 Nagahama, T., Mizuno, A., Ogawa, H., & Fukui, Y. 1998, *ApJ*, 116, 336  
 Nakajima, T., et al. 2007, *PASJ*, 59, 1005  
 Nakamura, F., et al. 2012, *ApJ*, 746, 25  
 Nishimura, A., et al. 2015, *ApJS*, 216, 1  
 Oka, T., Hasegawa, T., Hayashi, M., Handa, T., & Sakamoto, S. 1998, *ApJ*, 493, 730  
 Penzias A. A., & Burrus C. A. 1973, *ARA&A*, 11, 51  
 Peterson, D. E., & Megeath, S. T., 2008, *Handbook of Star Forming Regions*, Vol. I, The Northern Sky, ed. B. Reipurth (San Francisco: ASP), 590  
 Sakamoto, S., Hayashi, M., Hasegawa, T., Handa, T., & Oka, T. 1994, *ApJ*, 425, 641  
 Schöier, F. L., van der Tak, F. F. S., van Dishoeck, E. F., & Black, J. H. 2005, *A&A*, 432, 369  
 Schulz, A., et al. . *A&A*, 295, 183  
 Seta, M., Nakai, N., Ishii, S., Nagai, M., Miyamoto, Y., Ichikawa, T., Takato, N., & Motoyama, H. 2012, in *IAU Symp. 288, Astrophysics from Antarctica*, ed. M. G. Burton et al. (Cambridge: Cambridge University Press), 251  
 Shimajiri, Y., et al. 2011, *PASJ*, 63, 105  
 Tielens, A. G. G. M., & Hollenbach, D. 1985, *ApJ*, 291, 747  
 Ulich, B. L., & Haas, R. W. 1976, *ApJS*, 30, 247  
 Wilson, B. A., Dame, T. M., Masheder, M. R. W., & Thaddeus, P. 2005, *A&A*, 430, 523  
 Yoda, T., et al. 2010, *PASJ*, 62, 1277